Second-Order Nonlinear Optical Properties of an Amphiphilic Dye Embedded in a Lipid Bilayer. A Combined Molecular Dynamics-Quantum Chemistry Study

Bouquiaux, Charlotte; Tonnelé, Claire; Castet, Frédéric; Champagne, Benoît

Published in:
The Journal of Physical Chemistry. B, Condensed matter, materials, surfaces, interfaces & biophysical

DOI:
10.1021/acs.jpcb.9b10988

Publication date:
2020

Document Version
Publisher's PDF, also known as Version of record

THE JOURNAL OF PHYSICAL CHEMISTRY B

pubs.acs.org/JPCB Article

Second-Order Nonlinear Optical Properties of an Amphiphilic Dye Embedded in a Lipid Bilayer. A Combined Molecular Dynamics–Quantum Chemistry Study

Charlotte Bouquiaux, Claire Tonnelé, Frédéric Castet, and Benoît Champagne*

Cite This: *J. Phys. Chem. B* 2020, 124, 2101–2109 Read Online

ACCESS | Metrics & More | Article Recommendations | Supporting Information

ABSTRACT: The second harmonic signal of an amphiphilic dye embedded in a lipid bilayer has been calculated by combining molecular dynamics simulations and quantum chemistry calculations based on density functional theory. This computational approach provides insight into the morphology and dynamics of the fully hydrated biological system and the relationships linking the geometry and the environment of the dye to the amplitude of its second-order nonlinear optical response. The results point out a significant enhancement of the dynamic first hyperpolarizability of the dye induced by its interaction with the membrane and highlight the relative importance of dynamical, steric, and electrostatic effects. This computational scheme is thus particularly relevant for rationalizing the nonlinear optical contrasts revealed by second harmonic imaging microscopy of exogenous dyes embedded in biological media.

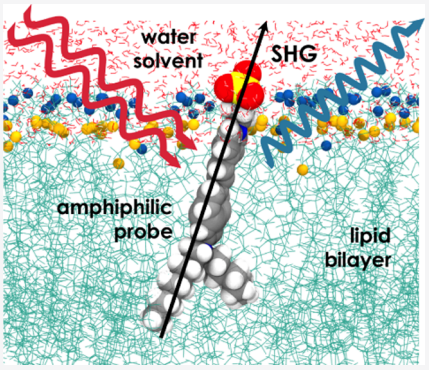

1. INTRODUCTION

The cell membrane is at the heart of many biological processes: without membranes, life as we know it would not be possible. A membrane is a selective semipermeable barrier separating cellular compartments that acts as a transporter.[1] Furthermore, transmembrane ionic gradients (mainly involving Na^+, K^+, and Cl^- ions) create a membrane potential that in turn provides an electrical driving force for many biological mechanisms.[1,2] The fundamental functions of membranes are dictated by their compositions:[1] lipids represent approximatively 50% in mass of most animal biomembranes, the rest being mostly proteins.[3] Amongst lipids, there is an enormous diversity of structures owing to the variety of fatty acids, their linkage positions, and their headgroups.[4] Interestingly, changes in lipid composition have been reported in numerous diseases.[1,4] The structure of lipid bilayers is described as fluid and flexible because of the possible motions of lipid molecules. These motions include rotations around the lipid long axes, "wiggles" of the fatty acids chains, translations within one layer, and motions to the other layer.[1,3]

As a matter of fact, the investigation of the structure and dynamics of a membrane is of particular importance. However, most biomolecules possess only few natural moieties with exploitable optical properties[5]—with the exception of structural proteins such as collagen[6,7] and cellulose[8]—so that exogenous dyes are often employed to improve the contrast in tissues for being detected by commercially available microscopes. Among the linear and nonlinear optical (NLO) phenomena operating in microscopy, fluorescence and second harmonic generation (SHG) are two main techniques whose combined use provides complementary information.[9−11] These optical processes differ by the nature of the initial and final molecular electronic states, and depend on the illumination wavelengths and intensities. Aminonaphtylethenylpyridinium (ANEP) dyes, like di-8-ANEPPS (Figure 1) developed by Loew and colleagues,[12,13] are often used in this context as labeling agents. These push−pull compounds are not only fluorescent probes, but also exhibit SHG responses.

SHG is a second-order NLO process, first demonstrated by Franken et al.[14] in crystalline quartz in 1961. It was then developed by Shen,[15] Eisenthal,[16] and others for the study of surfaces and artificial monolayers. The use of SHG in microscopy was proposed by Sheppard et al.[17] in 1977. Since then, there has been an expansion in the use of second harmonic imaging microscopy (SHIM), partially thanks to advances in laser technology.[18] SHG presents several advantages over fluorescence:[19] (i) it is intrinsically specific to interfacial regions, making it an ideal technique to study the biophysics of model membranes. Indeed, the observed signal is only due to non-centrosymmetrical molecules and molecular assemblies, whereas in fluorescence, a background is usually observed arising also from isotropic regions; (ii) the wave-

Received: November 24, 2019
Revised: February 26, 2020
Published: February 27, 2020

https://dx.doi.org/10.1021/acs.jpcb.9b10988
J. Phys. Chem. B 2020, 124, 2101–2109

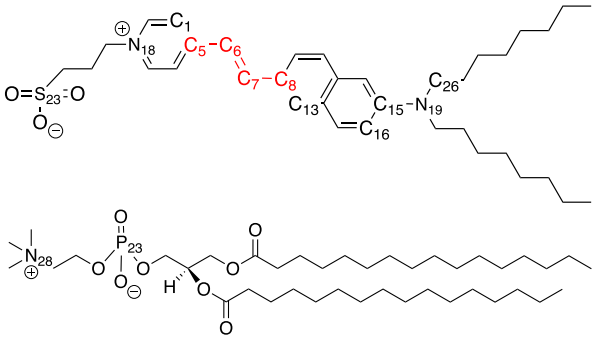

Figure 1. Structure of di-8-ANEPPS (top) and DPPC (bottom) with key atoms labeling, segment used to define the BLA (BLA = $1/2[d_{C_5-C_6} - 2d_{C_6-C_7} + d_{C_7-C_8}]$) of di-8-ANEPPS (red), and atoms used to define its torsion angles [$\theta_1 = \theta(C_1-C_5-C_6-C_7)$, $\theta_2 = \theta(C_6-C_7-C_8-C_{13})$, and $\theta_3 = \theta(C_{16}-C_{15}-N_{19}-C_{26})$].

length of 1064 nm commonly used in SHG measurements should prevent photodamage and photobleaching; (iii) the SHG signal retains the phase and directional data after interaction with the sample. Information about the molecular organization of the chromophore can therefore be extracted from SHG imaging data, by taking advantage of the SHG polarization anisotropy;[20] and (iv) finally, the SHG intensity can be modulated by an applied electric field,[21] and therefore be used as an efficient probe of the membrane potential.

SHG responses of biological systems have been widely studied throughout the literature.[8,18,20,22−32] In particular, a lot of works focused on the study of the transmembrane potential.[21,33−37] However, although several computational approaches allowing to predict and interpret macroscopic SHG responses of solutions,[38,39] periodic solids,[40−45] interfaces,[46] and self-assembled monolayers[47,48] have so far been developed, much less has been done for complex dynamical systems like dyed lipid bilayers. Few theoretical chemistry studies have also been performed to assess their SHG responses but either they truncate the chromophore complex surrounding, they do not account for geometry relaxation effects because of this surrounding, they rely on low-level methods to evaluate the β tensor components, or even they do not account for the dynamics of the system.[30,49−52]

On this basis, our global objective is to better understand the SHG responses of chromophores in lipid bilayers and to develop appropriate computational methods to unravel SHIM signatures. We focus in this report on the elaboration of a two-step simulation procedure and its application for a model system composed of a di-8-ANEPPS probe inserted into a hydrated 1,2-dipalmitoylphosphatidylcholine (DPPC) membrane. Molecular dynamics (MD) simulations are first performed to investigate the morphology of the ANEPPS@DPPC system and the dynamics of the chromophore inserted into the membrane. Then, the first hyperpolarizability (β) responses of the di-8-ANEPPS probe are evaluated using density functional theory (DFT) for selected snapshots extracted from the MD simulations. This computational approach provides insights into the relationships linking the geometry of the chromophore to the amplitude of its SHG responses and the related visible absorption spectra, into the impact of structural dynamics, and into the effects of the lipid bilayer environment.

2. COMPUTATIONAL AND THEORETICAL METHODS

2.1. MD Simulations. MD simulations of the ANEPPS@DPPC system were carried out using NAMD2.12,[53] whereas VMD1.9.4[54] was used for data visualization and analysis. The system consists of one di-8-ANEPPS dye molecule inserted into a lipid bilayer formed by 125 DPPC molecules (61 and 64 in the leaflet with and without the chromophore, respectively) and 3840 water molecules (see Figure 2), providing a

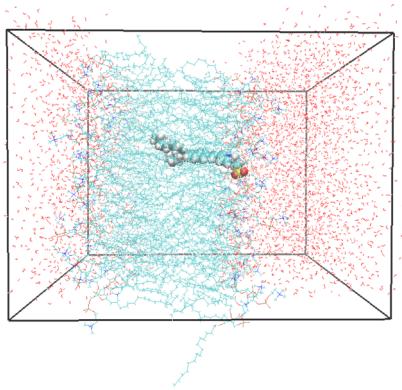

Figure 2. Simulation box containing 125 DPPC, the di-8-ANEPPS chromophore, and 3840 water molecules.

3840/125 = 30.72 water/lipid number ratio. This ratio corresponds to a weight content $c = m_{H_2O}/(m_{H_2O} + m_{DPPC})$ = 0.42. Note that experimental DPPC bilayers in the L_α phase are fully hydrated for c = 0.36[55,56] or c = 0.40.[57]

After the starting structure was generated using Packmol,[58] the system was modeled following a procedure similar to those commonly used in the literature, and described hereafter.[19,49,59−74] The partial charges were calculated for the chromophore, the water, and the lipid molecules using the electrostatic potential (ESP) model[75,76] at the DFT/M06-2X level with the cc-pVDZ basis set, as implemented in the Gaussian 16 package.[77] Periodic boundary conditions were applied in all three directions, so that the simulation is actually that of a multilamellar system. After an initial minimization of a low-density sample (with a starting box side of 80 Å), the ANEPPS@DPPC system was equilibrated for 140 ns in the *NPT* ensemble (P = 1 atm and T = 315.15 K[57]). This temperature was selected to ensure that the bilayer adopts the liquid crystalline (L_α) phase, the L_β to L_α phase transition temperature of DPPC being 315 K (see Section 1.3 in Supporting Information). A 240 ns production with a time step of 1 fs was then performed under the same conditions. The pressure and temperature were maintained using the Langevin piston[78] and Langevin temperature bath, respectively. Lennard-Jones interactions were truncated at 12 Å using a switching function starting at 10 Å, whereas long-range Coulombic interactions were treated using the particle-mesh Ewald technique.[79]

Given the high sensitivity of the β responses to the molecular geometry, a modified version of the general AMBER force field (GAFF)[80] was prepared to ensure an accurate description of the equilibrium geometry and torsional degrees of freedom of the di-8-ANEPPS molecule. As detailed in the Supporting Information, atom types and force constants were finely tuned in the force field (FF) in order to accurately reproduce the bond lengths of the DFT equilibrium structure

https://dx.doi.org/10.1021/acs.jpcb.9b10988
J. Phys. Chem. B 2020, 124, 2101−2109

and the associated bond length alternation (BLA), which is a prerequisite for reliably describing the NLO responses of push−pull π-conjugated compounds. Relaxed potential energy scans were computed at the M06-2X/cc-pVDZ level on a reduced fragment of di-8-ANEPPS, and fitted following the procedure described in ref 81.

Lipid molecules of the DPPC bilayer were described using the CHARMM 36[68,82] (C36) FF, whereas the SPC/Fw[83] FF was used for water molecules. The quality of the solvent description was verified in terms of density (1.06 g cm^{-3} against 1.00 g cm^{-3} for the experimental value) and radial distribution function (see Section 1.2 in the Supporting Information).

2.2. Calculation of the First Hyperpolarizability. Calculations of the static and dynamic NLO responses were performed at the time-dependent DFT (TDDFT)/M06-2X/6-311+G* level using the Gaussian 16[77] package. Frequency-dependent calculations were carried out using an incident wavelength of 1064 nm. We focused in this work on the hyper-Rayleigh scattering (HRS) response, β_{HRS}, and the associated depolarization ratio (DR), which are associated respectively to the second harmonic light intensity and to the symmetry of the molecular scatterer. Full expressions of these terms can be found in ref 84. In the case of the di-8-ANEPPS molecule embedded in the membrane, we also analyzed the diagonal β_{ZZZ} component of the first hyperpolarizability tensor, with Z the direction normal to the bilayer.

The NLO response of the isolated di-8-ANEPPS molecule (i.e., noninteracting with the membrane) was computed in the gas phase and in water using the integral equation formalism (IEF) of the polarizable continuum model (PCM).[85−87] To evaluate the NLO response of the di-8-ANEPPS molecule inserted into the membrane while accounting for the dynamical fluctuations of its geometry, 120 structures containing both the chromophore and the lipid bilayer were extracted from uncorrelated snapshots of the MD production run (every 2 ns). M06-2X/6-311+G* calculations were subsequently carried out on the 120 structures of the di-8-ANEPPS molecule, each being surrounded by ESP[75,76] charges of the neighboring lipids in order to account for electrostatic environment effects. Each lipid possessing at least one atom in a 5 Å radius defined around any atom of di-8-ANEPPS was considered entirely. The water solvent surrounding the ANEPPS@DPPC system was accounted for using IEFPCM.

In addition, to relate the nonlinear to the linear optical properties, the vertical excitation energies and transition dipoles of the low-lying excited states of the di-8-ANEPPS molecule were also calculated at the TDDFT/M06-2X/6-311+G* level. The computed first hyperpolarizabilities were rationalized by relying on the two-state approximation (TSA),[88] which assumes that only one electronic excited state (here, generally the S_2 state) contributes to the sum-over-state expansion of the second-order NLO response

$$\beta_{TSA} \propto \frac{\mu^2 \Delta\mu}{\Delta E^2} \times \frac{\Delta E^4}{[\Delta E^2 - (\hbar\omega)^2][\Delta E^2 - (2\hbar\omega)^2]} \quad (1)$$

where $\hbar\omega$ is the energy of the incident photons, ΔE is the $S_0 \rightarrow S_2$ excitation energy, $\mu = \|\langle S_0|\vec{\mu}|S_2\rangle\|$ is the norm of the associated transition dipole, and $\Delta\mu = \|\vec{\mu}_{S_2} - \vec{\mu}_{S_0}\|$ is the norm of the dipole moment variation between the S_0 and S_2 electronic states.

3. RESULTS AND DISCUSSION

3.1. Morphology of the ANEPPS@DPPC System. Several structural parameters have been evaluated to characterize the membrane, namely, the average area per lipid $\langle A \rangle$, the membrane thickness, the tilt angle of DPPC (including the lipid chains and polar head), and the hydrocarbon chain order parameter. Full details on these parameters and their calculations are provided in the Supporting Information. An average area per lipid of 56.3 ± 1.6 Å^2 is obtained for the leaflet without the chromophore, which is in the range predicted experimentally. The membrane thickness, measured as the average distance between the phosphorous atoms in the two bilayer leaflets amounts to 39.3 ± 0.3 Å^2, in good agreement with previously reported data (see the Supporting Information for details).[89]

Given the nature of its constituent moieties and overall flexibility of the DPPC molecules, three tilt angles were defined to get full insight into their orientation, namely θ_{P-N} defined between the phosphate group and the nitrogen atom of the choline group in the polar head, and two θ_{C-C} angles giving the orientation of the lipid alkyl chains (Supporting Information, Figure S7a,b). For θ_{P-N}, an average value of 76.0 ± 3.1° is obtained (Supporting Information, Figure S8a). This large angle allows for favorable interactions between the glycerol moieties and the water layer. The magnitude of the tilt angle is indeed controlled by the balance between the need for efficient hydrocarbon chain packing and the hydrophilic character of the polar head group.[90] In relatively good agreement with experimental measurements reported in the literature,[91] an average value 27.0 ± 3.1° is computed for θ_{C-C} (see the Supporting Information, Figure S8b), indicating a preferential orientation along the normal to the surface toward the interior of the membrane. Our description of the membrane is further validated by an hydrocarbon chain order parameter of 0.225 ± 0.003, fully consistent with the experimental value of 0.20 ± 0.02, which is characteristic of the L_α phase.[92]

The di-8-ANEPPS chromophore tends to orient preferentially along the normal to the membrane interface, with its polar head group interacting with the hydrophilic part of the lipid while alkyl tails pointing towards the hydrophobic interior of the membrane. A more detailed picture is provided by the analysis of the tilt angle θ_{N-N} of the long molecular axis with respect to the normal of the membrane plane (Figure 3a). A value of 90° indicates a parallel orientation of the

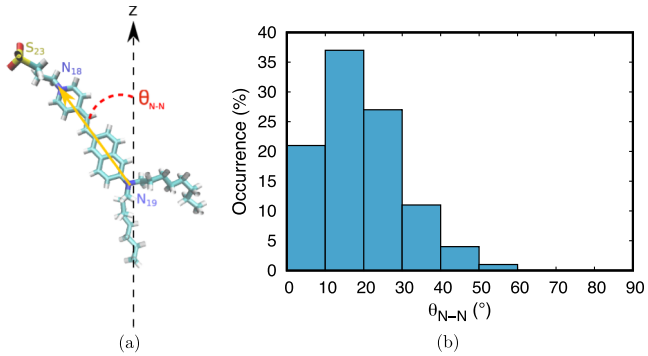

Figure 3. (a) Definition of the θ_{N-N} tilt angle between the vector connecting the N_{18} and N_{19} atoms and the normal to the bilayer interface (Z axis) and (b) distribution of θ_{N-N} (°) over the whole MD run.

https://dx.doi.org/10.1021/acs.jpcb.9b10988
J. Phys. Chem. B 2020, 124, 2101−2109

chromophore with respect to the membrane surface, whereas values of 0 and 180° correspond to perpendicular arrangements. The distribution of θ_{N-N} (Figure 3b) reflects the dynamical fluctuations, with values spanning a range of about 50°. The average tilt angle over the whole production run amounts to 19.3 ± 10.6°, confirming a quasi vertical orientation of the probe in the lipid bilayer. Alternative analyses of the chromophore tilt angle were performed by considering $\cos(\theta_{N-N})$ instead of θ_{N-N} as well as their violin plots with interquartile ranges (Figures S9 and S10) and they all conclude about the tilt of the chromophore. This global orientation of the di-8-ANEPPS molecule within the bilayer seems to be dictated by the lipid alkyl chains, which are also globally tilted (by 27.0 ± 3.1°) with respect to the bilayer normal. A very similar distribution is obtained on the 120 frames used for the subsequent evaluation of the NLO response, with an average value of 18.9 ± 10.7°, confirming that it constitutes a representative set of structures.

Mass density profiles of the relevant components of the system have also been calculated to get insight into their relative position, and are displayed in Figure 4. Besides confirming the orientation of the chromophore in the membrane and its location in only one DPPC leaflet, these results indicate that the SO_3 (S_{23}) moiety of the probe is located in the region occupied by the polar headgroup of the DPPC (N_{28} and P_{23}) as well as by water molecules, whereas the chromophore extends into the hydrophobic fatty acids. This picture is consistent with the limited variations observed in the value of the di-8-ANEPPS molecular tilt angle.

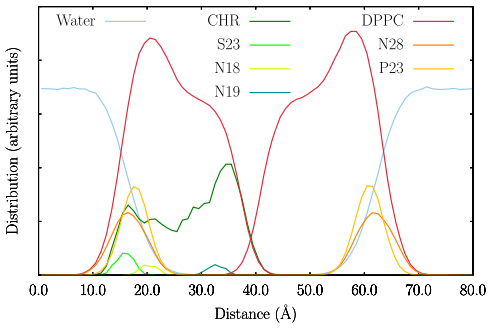

Figure 4. Mass density profiles along the Z axis for the different components of the ANEPPS@DPPC system: DPPC (red) and its N_{28} (orange) and P_{23} (yellow) atoms, chromophore (CHR, dark green) and its S_{23} (light green), N_{18} (yellowish green), and N_{19} (dark blue) atoms, and water molecules (light blue).

3.2. NLO Response of the Chromophore within the Lipid Bilayer. Figure 5 presents the time evolution of the static and dynamic β_{ZZZ} hyperpolarizability components, as well as of their cumulative averages. Even though individual values vary strongly over time, the cumulative averages rapidly converge. The average static β_{ZZZ} amounts to 65 × 10^3 ± 15 × 10^3 a.u., whereas frequency dispersion effects enhance the NLO response by 1 order of magnitude, with β_{ZZZ} = 510 × 10^3 ± 418 × 10^3 a.u. This large standard deviation highlights the influence of the dynamical structural changes on the dynamic first hyperpolarizability. However, it is notably amplified by a few extreme β_{ZZZ} values ranging between 1500 × 10^3 and 3000 × 10^3 a.u. When excluding these structures from the statistics, the average dynamic β_{ZZZ} and its standard deviation reduces to 444 × 10^3 ± 217 × 10^3 a.u., which is still seven times larger than the static ones. These larger β_{ZZZ} responses are the consequence of resonant or near-resonant conditions, as confirmed by TDDFT/M06-2X/6-311+G* calculations of the excitation energies. Structures exhibiting intense NLO responses all display excitation wavelengths close to 532 nm, which corresponds to the second harmonic wavelength of a 1064 nm incident beam. Still, they are only a few, as shown by their distribution and the resulting visible absorption spectrum (Figure 6). Note that, although technological applications

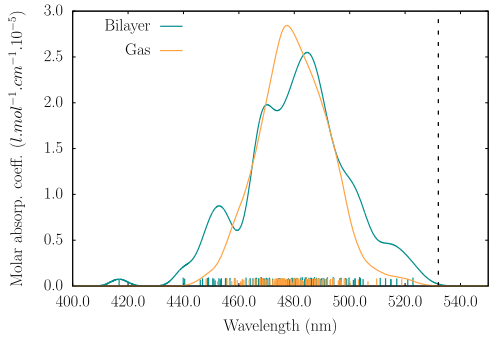

Figure 6. Distribution of the lowest energy dipole-allowed excitation energies and oscillator strengths of the chromophore surrounded by lipid charges and implicit solvent molecules and visible absorption spectrum as obtained from their convolution with Gaussian functions having full width at half-maximum of 0.05 eV, in comparison to their analogs obtained without accounting for the effects of the surrounding (gas) while keeping the same geometries. The calculations were performed at the TDDFT/M06-2X/6-311+G* level. The vertical dashed line corresponds to the energy of the SHG photons.

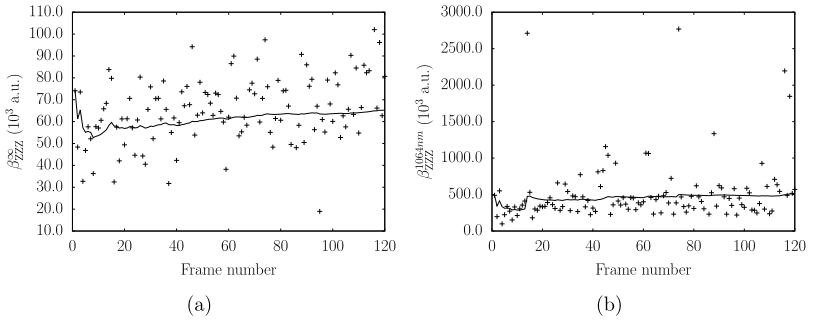

Figure 5. Time evolution of β_{ZZZ} (10^3 a.u.) [cross] and its cumulative average [line] for the chromophore surrounded by lipid charges and implicit solvent molecules, as calculated at the IEFPCM/TDDFT/M06-2X/6-311+G* level. (a) $\lambda = \infty$ and (b) λ = 1064 nm.

https://dx.doi.org/10.1021/acs.jpcb.9b10988
J. Phys. Chem. B 2020, 124, 2101−2109

might take advantage of resonance-enhanced NLO responses, excitation-induced electron density redistributions can lead to photodamages and should be avoided for biological applications.

A linear correlation was also unravelled between the $\beta_{ZZZ}^{1064nm}/\beta_{ZZZ}^{\infty}$ ratio and the first dipole-allowed excitation energy ΔE of the chromophore, or more specifically the dispersion factor at the second harmonic frequency, defined as $1/(\Delta E - 2\hbar\omega)$ with $\hbar\omega$ the energy of the incident photons (Figure 7). This strong correlation demonstrates that the two state model describes most of the frequency dispersion effects of β_{ZZZ}.

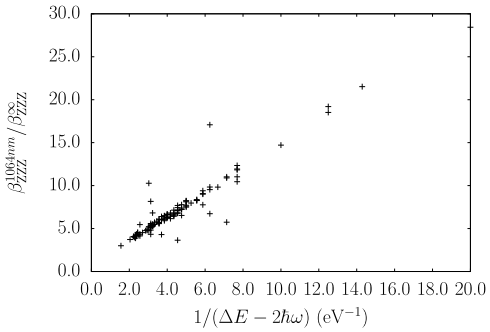

Figure 7. Evolution of the $\beta_{ZZZ}^{1064nm}/\beta_{ZZZ}^{\infty}$ ratio as a function of the excitation energy (ΔE, eV) of the chromophore. For readability, few resonant frames were not included. The β and ΔE values were calculated at the IEFPCM/TDDFT/M06-2X/6-311+G* level for the chromophore surrounded by the lipid charges and implicit solvation. $\hbar\omega$ is the energy of the incident photons.

3.3. Structure–Property Relationships. In this section, we decipher the relationships between the structure of the chromophore and its NLO response. By definition, the normal β_{ZZZ} component discussed above is expected to depend on the orientation of the chromophore within the bilayer, which is characterized by the θ_{N-N} angle (Figure 3). The correlation between β_{ZZZ} and θ_{N-N} is evidenced in Figure 8a, where the third power of $\cos(\theta_{N-N})$ is used as abscissa because β is a rank-3 tensor. The correlation plot confirms that small β_{ZZZ} values are associated with large θ_{N-N} angles.

To establish structure–property relationships that are independent of the orientation of the chromophore within the lipid bilayer (or at least to reduce the orientational effects), the focus switches now from β_{ZZZ} to β_{HRS}, which accounts for averages over molecular orientations. Figure 8b shows the correlation between $\beta_{ZZZ}/\cos^3(\theta_{N-N})$, which approximates a hypothetical tilt-independent normal β tensor component, and the β_{HRS} values. Overall, these two quantities are strongly correlated (with a correlation coefficient $R^2 = 0.95$), which indicates the adequacy of considering β_{HRS} for further analyses.

Like for β_{ZZZ}, the time evolutions for the static and dynamic β_{HRS} values given in Figure 9 also exhibit strong variations, whereas their cumulative averages rapidly converge. The average static β_{HRS} amounts to $35 \times 10^3 \pm 7 \times 10^3$ a.u., whereas at 1064 nm it is more than three times larger and attains $125 \times 10^3 \pm 40 \times 10^3$ a.u. Then, the average static and dynamic DR amount to 4.88 ± 0.02 and 4.99 ± 0.01, respectively, and are typical of one-dimensional π-conjugated push–pull molecules. The small standard deviation on DR indicates that it is virtually unaffected by the dynamical nature of the system, which can be correlated to the small departures of the di-8-ANEPPS geometry from planarity (vide infra) along the dynamics.

Then, we assess how the dynamical fluctuations in the geometry of the chromophore affect the β_{HRS} response, focusing in particular on two structural parameters, namely, the BLA and the torsional angles θ_{1-3}, as defined in Figure 1. Average values and standard deviations are reported in Table 1, whereas individual values are reported in the Supporting Information (Figure S13a–d). Our simulation shows a rather small BLA value of 0.06 ± 0.03 Å, consistent with the DFT geometry used for the FF parametrization, and associated with a strong π-electron delocalization between the donor and acceptor groups. However, about 20% of the extracted structures exhibit a value outside the "one standard deviation" range (Figure S13a). Whereas some of them can be linked to extreme values of β_{HRS}, there is no global correlation between the two quantities, as shown in Figure S14a. Moreover, along the simulation, the chromophore deviates from planarity with average out-of-plane distortions of about 10°. Here also, extreme values of the torsional angles are observed, but no correlation is found between β_{HRS} and any of the investigated dihedrals (see Figure S14b–d). The lack of correlation between β_{HRS} and the selected structural parameters indicates that the variations in the NLO response cannot be ascribed to the dynamical fluctuations of a single parameter, but result from global distortions of the molecular structure. Note also that the fluctuations of β values can also be induced by variations of the lipid environment (i.e., of the position of the ESP charges surrounding the chromophore), which makes the analysis even more complex.

3.4. Environment Effects. In this part, we analyze the influence of the environment on the NLO responses of the di-8-ANEPPS molecule. In Table 2, the β_{HRS} and DR values computed for the isolated chromophore or within an implicit water solvent using the DFT or GAFF equilibrium geometries

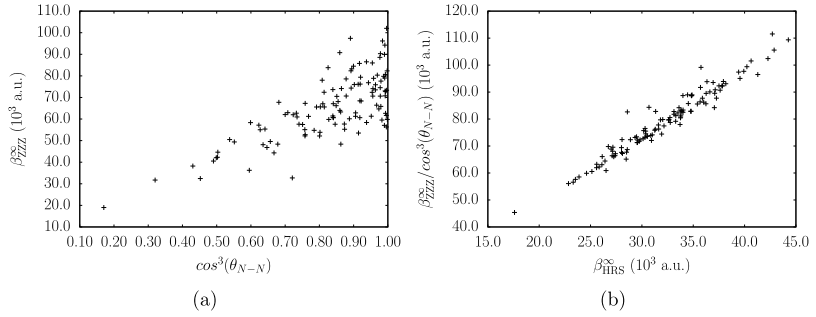

Figure 8. (a) Static β_{ZZZ} (10^3 a.u.) as a function of $\cos^3(\theta_{N-N})$ and (b) relationship between $\beta_{ZZZ}/\cos^3(\theta_{N-N})$ and β_{HRS} (both in 10^3 a.u.).

https://dx.doi.org/10.1021/acs.jpcb.9b10988
J. Phys. Chem. B 2020, 124, 2101–2109

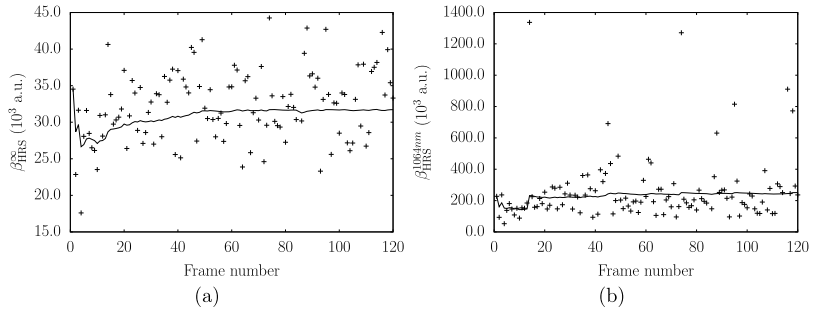

Figure 9. Time evolution of β_{HRS} (10^3 a.u.) [cross] and its cumulative average [line] for the chromophore surrounded by lipid charges and implicit solvent molecules, as calculated at the IEFPCM/TDDFT/M06-2X/6-311+G* level. (a) $\lambda = \infty$ and (b) $\lambda = 1064$ nm.

Table 1. Average Values and Standard Deviations of the BLA (Å) and of the Dihedral Angles (°) of Di-8-ANEPPS Calculated over the 120 Snapshots Extracted from the MD Simulation of the ANEPPS@DPPC System

BLA	θ_1	θ_2	θ_3
0.06 ± 0.03	171.4 ± 7.4	170.8 ± 7.1	170.4 ± 6.2

are compared with those calculated on structures extracted from MD simulations. The latter account for the structural dynamics of the system and include the electrostatic effects due to the lipid bilayer. Environmental effects are first highlighted by the large increase of the static β_{HRS} and the small decrease of the dynamic β_{HRS} when going from the gas phase to the implicit aqueous phase (19×10^3 vs 32×10^3 a.u. and 86×10^3 vs 80×10^3 a.u., respectively). This is attributed to the much larger static dielectric constant of water, in comparison to its optical one, which enhances the push−pull character of the chromophore.

Then, moving to the bilayer environment leads to a substantial increase of the dynamic β_{HRS}, from 97×10^3 to $255 \times 10^3 \pm 198 \times 10^3$ a.u., which highlights both the specific effects of the environment and of the dynamical behavior. Comparison with additional gas phase β_{HRS} calculations on the MD structures (Figure S15 in the Supporting Information) demonstrates that (i) in the static limit β_{HRS} is almost not impacted by structural dynamics ($\beta_{HRS} = 19 \times 10^3 \pm 2 \times 10^3$ a.u. from MD vs 20×10^3 a.u. for the equilibrium structure) but its variations originate from the polarization because of the surrounding ($\beta_{HRS} = 32 \times 10^3 \pm 5 \times 10^3$ a.u. in the bilayer vs $19 \times 10^3 \pm 2 \times 10^3$ a.u. for the isolated chromophore) while (ii) at $\lambda = 1064$ nm, the dynamical behavior plays also a role, which is attributed to the variations of the excitation energies and the presence of near-resonance situations. In fact, when only accounting for the dynamical structural behavior of the chromophore in the bilayer, which anyway is constrained by the DPPC molecules of the bilayer, the dynamic β_{HRS} increases from 97×10^3 to $170\ 10^3 \pm 88 \times 10^3$ a.u. Then, when taking into account the effects of the surrounding on the β_{HRS} calculations, the latter further increases from $170 \times 10^3 \pm 88 \times 10^3$ to $255 \times 10^3 \pm 198 \times 10^3$ a.u. This second effect is consistent with the modifications of the visible absorption spectrum of the chromophore, which gets broader and exhibits a vibronic-like structure when accounting for the bilayer surrounding (Figure 6). In particular, the latter is responsible for an increased absorption intensity close to the SHG wavelength. Note that the corresponding excitation energy of the chromophore in its rpGAFF ground-state equilibrium structure is even larger and attains 2.79 eV, in comparison to the maximum absorption energies of 2.55 and 2.60 eV for the MD structures with and without the bilayer surrounding, respectively. Finally, all DR values are very close to 5, the typical value of one-dimensional push−pull π-conjugated compounds but still, accounting for the bilayer environment reduces strongly the standard deviation (see also Figure S16 in the Supporting Information).

The striking increase of β_{HRS} after inclusion of the molecular probe into the lipid bilayer is particularly relevant for SHIM because it demonstrates that the surrounding has no detrimental effect on the SHG signal but, on the contrary, it enhances it.

Table 2. Static and Dynamic ($\lambda = 1064$ nm) β_{HRS} (10^3 a.u.) and DR of Di-8-ANEPPS, Calculated at the TDDFT/M06-2X/6-311+G* Level for Different Structures, Either Corresponding to (Ground State) Equilibrium Geometries or Obtained from MD Simulations[a]

			static		dynamic	
structures(s)	geometries[b]	surrounding[c]	β_{HRS}	DR	β_{HRS}	DR
equilibrium	DFT	isolated	19	4.88	86	4.98
equilibrium	DFT	IEFPCM	32	4.83	80	4.97
equilibrium	standard GAFF	isolated	9	4.73	31	4.88
equilibrium	rpGAFF	isolated	20	4.87	97	4.98
MD	rpGAFF	isolated	19 ± 2	4.77 ± 0.10	170 ± 88	4.89 ± 0.33
MD	rpGAFF	bilayer	32 ± 5	4.88 ± 0.02	255 ± 198	4.99 ± 0.01

[a]In the former case, the β calculations were performed for the isolated molecule or by accounting for solvent (water) effects using the IEFPCM scheme, whereas in the latter case, they were performed with or without accounting for the bilayer environment. [b]Level of approximation for optimizing the geometries. [c]Treatment of the surrounding in β_{HRS} calculations.

https://dx.doi.org/10.1021/acs.jpcb.9b10988
J. Phys. Chem. B 2020, 124, 2101−2109

4. CONCLUSIONS AND OUTLOOK

A combined MD−quantum chemistry method has been elaborated to investigate the embedding effects on the first hyperpolarizability of an amphiphilic dye in a lipid bilayer. The system consists of di-8-ANEPPS, a typical ANEP dye in a hydrated DPPC membrane. The method associates MD simulations where classical FFs are employed with TDDFT calculations to evaluate the first hyperpolarizability of the dye in the charge electric field because of the surrounding lipids. Still, the FF of the dye had to be re-parameterized with respect to DFT geometries in order to account for the strong dependence of the first hyperpolarizability on the molecular geometry. The results highlight (i) the huge increase of the first hyperpolarizability of the dye when inserted into the bilayer lipids, (ii) the double origin of this enhancement resulting both from the dynamical structural flexibility of the chromophore and from the polarization of the bilayer surrounding, (iii) the orientational motions of the dye in the bilayer, of which the backbone axis is tilted by about 20 ± 10° with respect to the bilayer normal, (iv) the relationship between this tilt angle and β_{ZZZ}, the diagonal β tensor component oriented along the bilayer normal, (v) the one-dimensional NLOphore character of the dye, evidenced by DRs close to 5 and the validity of the two-state model, and (vi) the difficulty to relate the β_{ZZZ} and β_{HRS} values to single geometrical parameters of the dye like the BLA and the torsion angles.

These huge surrounding effects, which are beneficial for the SHIM technique call for further investigating the role of the nature of the lipid bilayer on the second-order NLO responses as well as on the variations of these responses as a function of external perturbations, like those created by membrane potentials. In particular, future works will focus on investigating the correlations between the SHG responses and the relative orientations of the chromophore and of the lipid chains. So, focusing on more and more complex systems will finally enable us to closely model real bilayers and to perform comparisons with experimental data.

■ ASSOCIATED CONTENT

Supporting Information

The Supporting Information is available free of charge at https://pubs.acs.org/doi/10.1021/acs.jpcb.9b10988.

Details on (i) the MD simulation (FF reparameterization for di-8-ANEPPS, assessment of the validity of the FF for water and the DPPC lipid bilayer) and on (ii) the NLO properties (structure−β relationships, gas phase β_{HRS} for the MD structures, and DR values for the MD structures) (PDF)

■ AUTHOR INFORMATION

Corresponding Author

Benoît Champagne − *Theoretical Chemistry Laboratory, Unit of Theoretical and Structural Physical Chemistry, Namur Institute of Structured Matter, University of Namur, B-5000 Namur, Belgium;* orcid.org/0000-0003-3678-8875; Email: benoit.champagne@unamur.be

Authors

Charlotte Bouquiaux − *Theoretical Chemistry Laboratory, Unit of Theoretical and Structural Physical Chemistry, Namur Institute of Structured Matter, University of Namur, B-5000 Namur, Belgium*

Claire Tonnelé − *University of Bordeaux, Institut des Sciences Moléculaires, UMR 5255 CNRS, F-33405 Talence Cedex, France;* orcid.org/0000-0003-0791-8239

Frédéric Castet − *University of Bordeaux, Institut des Sciences Moléculaires, UMR 5255 CNRS, F-33405 Talence Cedex, France;* orcid.org/0000-0002-6622-2402

Complete contact information is available at: https://pubs.acs.org/10.1021/acs.jpcb.9b10988

Notes

The authors declare no competing financial interest.

■ ACKNOWLEDGMENTS

C.B. thanks the F.R.S.-FNRS for her FRIA fellowship. The calculations were performed on the computers of the Consortium des Équipements de Calcul Intensif (CÉCI, http://www.ceci-hpc.be) and particularly those of the Technological Platform of High-Performance Computing, for which the authors gratefully acknowledge the financial support of the FNRS-FRFC, of the Walloon Region, and of the University of Namur (Conventions no. 2.5020.11, GEQ U.G006.15, 1610468, and RW/GEQ2016), and on zenobe, the Tier-1 facility of the Walloon Region (Convention 1117545).

■ REFERENCES

(1) *Medical Cell Biology*, 3rd ed.; Goodman, S. R., Ed.; Academic Press: San Diego, 2008; pp 27−57.

(2) Friedman, R. Membrane-Ion Interactions. *J. Membr. Biol.* **2018**, *251*, 453−460.

(3) Alberts, B.; Johnson, A.; Lewis, J. *The Lipid Bilayer from Molecular Biology of the Cell*, 4th ed.; Garland Science, 2002.

(4) Harayama, T.; Riezman, H. Understanding the Diversity of Membrane Lipid Composition. *Nat. Rev. Mol. Cell Biol.* **2018**, *19*, 281−296.

(5) Thomas, J. A. Optical Imaging Probes for Biomolecules: An Introductory Perspective. *Chem. Soc. Rev.* **2015**, *44*, 4494−4500.

(6) Freund, I.; Deutsch, M.; Sprecher, A. Connective tissue polarity. Optical second-harmonic microscopy, crossed-beam summation, and small-angle scattering in rat-tail tendon. *Biophys. J.* **1986**, *50*, 693−712.

(7) de Wergifosse, M.; de Ruyck, J.; Champagne, B. How the Second-Order Nonlinear Optical Response of the Collagen Triple Helix Appears: A Theoretical Investigation. *J. Phys. Chem. C* **2014**, *118*, 8595−8602.

(8) Malcom Brown, R., Jr.; Millard, A. C.; Campagnola, P. J. Macromolecular Structure of Cellulose Studied by Second-Harmonic Generation Imaging Microscopy. *Opt. Lett.* **2003**, *28*, 2207−2209.

(9) Moreaux, L.; Sandre, O.; Blanchard-Desce, M.; Mertz, J. Membrane Imaging by Simultaneous Second-Harmonic Generation and Two-Photon Microscopy. *Opt. Lett.* **2000**, *25*, 320−322.

(10) Zipfel, W. R.; Williams, R. M.; Christie, R.; Nikitin, A. Y.; Hyman, B. T.; Webb, W. W. Live Tissue Intrinsic Emission Microscopy using Multiphoton-Excited Native Fluorescence and Second Harmonic Generation. *Proc. Natl. Acad. Sci. U.S.A.* **2003**, *100*, 7075−7080.

(11) Millard, A. C.; Terasaki, M.; Loew, L. M. Second Harmonic Imaging of Exocytosis at Fertilization. *Biophys. J.* **2005**, *88*, L46−L48.

(12) Fluhler, E.; Burnham, V. G.; Loew, L. M. Spectra, Membrane Binding, and Potentiometric Responses of New Charge Shift Probes. *Biochemistry* **1985**, *24*, 5749−5755.

(13) Loew, L. M. Potentiometric Dyes: Imaging Electrical Activity of Cell Membranes. *Pure Appl. Chem.* **1996**, *68*, 1405−1409.

(14) Franken, P. A.; Hill, A. E.; Peters, C. W.; Weinreich, G. Generation of Optical Harmonics. *Phys. Rev. Lett.* **1961**, *7*, 118−119.
(15) Shen, Y. R. Surface Properties Probed by Second-Harmonic and Sum-Frequency Generation. *Nature* **1989**, *337*, 519−525.
(16) Eisenthal, K. B. Liquid Interfaces Probed by Second-Harmonic and Sum-Frequency Spectroscopy. *Chem. Rev.* **1996**, *96*, 1343−1360.
(17) Sheppard, C.; Gannaway, J.; Kompfner, R.; Walsh, D. The scanning harmonic optical microscope. *IEEE J. Quantum Electron.* **1977**, *13*, 912.
(18) Campagnola, P. J.; Wei, M.-d.; Lewis, A.; Loew, L. M. High-Resolution Nonlinear Optical Imaging of Live Cells by Second Harmonic Generation. *Biophys. J.* **1999**, *77*, 3341−3349.
(19) Reeve, J. E.; Anderson, H. L.; Clays, K. Dyes for Biological Second Harmonic Generation Imaging. *Phys. Chem. Chem. Phys.* **2010**, *12*, 13484−13498.
(20) Campagnola, P. J.; Millard, A. C.; Terasaki, M.; Hoppe, P. E.; Malone, C. J.; Mohler, W. A. Three-Dimensional High-Resolution Second-Harmonic Generation Imaging of Endogenous Structural Proteins in Biological Tissues. *Biophys. J.* **2002**, *82*, 493−508.
(21) Bouevitch, O.; Lewis, A.; Pinevsky, I.; Wuskell, J. P.; Loew, L. M. Probing Membrane Potential with Nonlinear Optics. *Biophys. J.* **1993**, *65*, 672−679.
(22) Moreaux, L.; Sandre, O.; Mertz, J. Membrane Imaging by Second-Harmonic Generation Microscopy. *J. Opt. Soc. Am. B* **2000**, *17*, 1685−1694.
(23) Moreaux, L.; Sandre, O.; Charpak, S.; Blanchard-Desce, M.; Mertz, J. Coherent Scattering in Multi-Harmonic Light Microscopy. *Biophys. J.* **2001**, *80*, 1568−1574.
(24) Campagnola, P. J.; Loew, L. M. Second-harmonic imaging microscopy for visualizing biomolecular arrays in cells, tissues and organisms. *Nat. Biotechnol.* **2003**, *21*, 1356−1360.
(25) Mohler, W.; Millard, A. C.; Campagnola, P. J. Second Harmonic Generation Imaging of Endogenous Structural Proteins. *Methods* **2003**, *29*, 97−109.
(26) Williams, R. M.; Zipfel, W. R.; Webb, W. W. Interpreting Second-Harmonic Generation Images of Collagen I Fibrils. *Biophys. J.* **2005**, *88*, 1377−1386.
(27) Millard, A. C.; Terasaki, M.; Loew, L. M. Second Harmonic Imaging of Exocytosis at Fertilization. *Biophys. J.* **2005**, *88*, L46−L48.
(28) Asselberghs, I.; Flors, C.; Ferrighi, L.; Botek, E.; Champagne, B.; Mizuno, H.; Ando, R.; Miyawaki, A.; Hofkens, J.; der Auweraer, M. V. d.; Clays, K. Second-Harmonic Generation in GFP-like Proteins. *J. Am. Chem. Soc.* **2008**, *130*, 15713−15719.
(29) Deniset-Besseau, A.; Duboisset, J.; Benichou, E.; Hache, F.; Brevet, P.-F.; Schanne-Klein, M.-C. Measurement of the Second-Order Hyperpolarizability of the Collagen Triple Helix and Determination of Its Physical Origin. *J. Phys. Chem. B* **2009**, *113*, 13437−13445.
(30) de Meulenaere, E.; Nguyen Bich, N.; de Wergifosse, M.; Van Hecke, K.; Van Meervelt, L.; Vanderleyden, J.; Champagne, B.; Clays, K. Improving the Second-Order Nonlinear Optical Response of Fluorescent Proteins: The Symmetry Argument. *J. Am. Chem. Soc.* **2013**, *135*, 4061−4069.
(31) Timr, Š.; Brabec, J.; Bondar, A.; Ryba, T.; Železný, M.; Lazar, J.; Jungwirth, P. Nonlinear Optical Properties of Fluorescent Dyes Allow for Accurate Determination of Their Molecular Orientations in Phospholipid Membranes. *J. Phys. Chem. B* **2015**, *119*, 9706−9716.
(32) Okur, H. I.; Tarun, O. B.; Roke, S. Chemistry of Lipid Membranes from Models to Living Systems: A Perspective of Hydration, Surface Potential, Curvature, Confinement and Heterogeneity. *J. Am. Chem. Soc.* **2019**, *141*, 12168−12181.
(33) Peleg, G.; Lewis, A.; Linial, M.; Loew, L. M. Nonlinear optical measurement of membrane potential around single molecules at selected cellular sites. *Proc. Natl. Acad. Sci. U.S.A.* **1999**, *96*, 6700−6704.
(34) Millard, A. C.; Jin, L.; Wei, M.-d.; Wuskell, J. P.; Lewis, A.; Loew, L. M. Sensitivity of Second Harmonic Generation from Styryl Dyes to Transmembrane Potential. *Biophys. J.* **2004**, *86*, 1169−1176.
(35) Dombeck, D. A.; Sacconi, L.; Blanchard-Desce, M.; Webb, W. W. Optical Recording of Fast Neuronal Membrane Potential Transients in Acute Mammalian Brain Slices by Second-Harmonic Generation Microscopy. *J. Neurophysiol.* **2005**, *94*, 3628−3636.
(36) Nuriya, M.; Jiang, J.; Nemet, B.; Eisenthal, K. B.; Yuste, R. Imaging membrane potential in dendritic spines. *Proc. Natl. Acad. Sci. U.S.A.* **2006**, *103*, 786−790.
(37) Nuriya, M.; Yasui, M. Membrane potential dynamics of axons in cultured hippocampal neurons probed by second-harmonic-generation imaging. *J. Biomed. Opt.* **2010**, *15*, 020503.
(38) Benassi, E.; Egidi, F.; Barone, V. General Strategy for Computing Nonlinear Optical Properties of Large Neutral and Cationic Organic Chromophores in Solution. *J. Phys. Chem. B* **2015**, *119*, 3155−3173.
(39) Pielak, K.; Tonnelé, C.; Sanguinet, L.; Cariati, E.; Righetto, S.; Muccioli, L.; Castet, F.; Champagne, B. Dynamical Behavior and Second Harmonic Generation Responses in Acido-Triggered Molecular Switches. *J. Phys. Chem. C* **2018**, *122*, 26160−26168.
(40) Reis, H.; Papadopoulos, M. G.; Munn, R. W. Calculation of macroscopic first-, second-, and third-order optical susceptibilities for the urea crystal. *J. Chem. Phys.* **1998**, *109*, 6828−6838.
(41) Kirtman, B.; Dykstra, C. E.; Champagne, B. Major Intermolecular Effects on Nonlinear Electrical Response in a Hexatriene Model of Solid State Polyacetylene. *Chem. Phys. Lett.* **1999**, *305*, 132−138.
(42) Champagne, B.; Bishop, D. M. *Advances in Chemical Physics*; John Wiley & Sons, Inc., 2003; Vol. *126*.
(43) Seidler, T.; Stadnicka, K.; Champagne, B. Investigation of the Linear and Second-Order Nonlinear Optical Properties of Molecular Crystals Within the Local Field Theory. *J. Chem. Phys.* **2013**, *139*, 114105.
(44) Rérat, M.; Maschio, L.; Kirtman, B.; Civalleri, B.; Dovesi, R. Computation of Second Harmonic Generation for Crystalline Urea and KDP. An ab Initio Approach through the Coupled Perturbed Hartree-Fock/Kohn-Sham Scheme. *J. Chem. Theory Comput.* **2016**, *12*, 107−113.
(45) Seidler, T.; Krawczuk, A.; Champagne, B.; Stadnicka, K. QTAIM-Based Scheme for Describing the Linear and Nonlinear Optical Susceptibilities of Molecular Crystals Composed of Molecules with Complex Shapes. *J. Phys. Chem. C* **2016**, *120*, 4481−4494.
(46) Licari, G.; Cwiklik, L.; Jungwirth, P.; Vauthey, E. Exploring Fluorescent Dyes at Biomimetic Interfaces with Second Harmonic Generation and Molecular Dynamics. *Langmuir* **2017**, *33*, 3373−3383.
(47) Tonnelé, C.; Pielak, K.; Deviers, J.; Muccioli, L.; Champagne, B.; Castet, F. Nonlinear optical responses of self-assembled monolayers functionalized with indolino-oxazolidine photoswitches. *Phys. Chem. Chem. Phys.* **2018**, *20*, 21590−21597.
(48) Tonnelé, C.; Champagne, B.; Muccioli, L.; Castet, F. Nonlinear Optical Contrast in Azobenzene-Based Self-Assembled Monolayers. *Chem. Mater.* **2019**, *31*, 6759−6769.
(49) Rusu, C. F.; Lanig, H.; Othersen, O. G.; Kryschi, C.; Clark, T. Monitoring Biological Membrane-Potential Changes: A CI QM/MM Study. *J. Phys. Chem. B* **2008**, *112*, 2445−2455.
(50) Murugan, N. A.; Apostolov, R.; Rinkevicius, Z.; Kongsted, J.; Lindahl, E.; Ågren, H. Association Dynamics and Linear and Nonlinear Optical Properties of an N-Acetylaladanamide Probe in a POPC Membrane. *J. Am. Chem. Soc.* **2013**, *135*, 13590−13597.
(51) Osella, S.; Murugan, N. A.; Jena, N. K.; Knippenberg, S. Investigation into Biological Environments through (Non)linear Optics: A Multiscale Study of Laurdan Derivatives. *J. Chem. Theory Comput.* **2016**, *12*, 6169−6181.
(52) de Wergifosse, M.; Botek, E.; de Meulenaere, E.; Clays, K.; Champagne, B. ONIOM Investigation of the Second-Order Nonlinear Optical Responses of Fluorescent Proteins. *J. Phys. Chem. B* **2018**, *122*, 4993−5005.
(53) Phillips, J. C.; Braun, R.; Wang, W.; Gumbart, J.; Tajkhorshid, E.; Villa, E.; Chipot, C.; Skeel, R. D.; Kalé, L.; Schulten, K. Scalable

https://dx.doi.org/10.1021/acs.jpcb.9b10988
J. Phys. Chem. B 2020, 124, 2101−2109

Molecular Dynamics with NAMD. *J. Comput. Chem.* **2005**, *26*, 1781−1802.
(54) Humphrey, W.; Dalke, A.; Schulten, K. VMD: Visual Molecular Dynamics. *J. Mol. Graphics* **1996**, *14*, 33−38.
(55) Ruocco, M. J.; Shipley, G. G. Characterization of the Sub-Transition of Hydrated Dipalmitoylphosphatidylcholine Bilayers. Kinetic, Hydration and Structural Study. *Biochim. Biophys. Acta* **1982**, *691*, 309−320.
(56) Inoko, Y.; Mitsui, T. Structural Parameters of Dipalmitoyl Phosphatidylcholine Lamellar Phases and Bilayer Phase Transitions. *J. Phys. Soc. Jpn.* **1978**, *44*, 1918−1924.
(57) Janiak, M. J.; Small, D. M.; Shipley, G. G. Nature of the Thermal Pretransition of Synthetic Phospholipids: Dimyristoyl- and Dipalmitoyllecithin. *Biochemistry* **1976**, *15*, 4575−4580.
(58) Martínez, L.; Andrade, R.; Birgin, E. G.; Martínez, J. M. Packmol: A Package for Building Initial Configurations for Molecular Dynamics Simulations. *J. Comput. Chem.* **2009**, *30*, 2157−2164.
(59) van der Ploeg, P.; Berendsen, H. J. C. Molecular Dynamics Simulation of a Bilayer Membrane. *J. Chem. Phys.* **1982**, *76*, 3271−3276.
(60) Feller, S. E.; Yin, D.; Pastor, R. W.; MacKerell, A. D., Jr. Molecular Dynamics Simulation of Unsaturated Lipid Bilayers at Low Hydration: Parameterization and Comparison with Diffraction Studies. *Biophys. J.* **1997**, *73*, 2269−2279.
(61) Marrink, S.-J.; Berger, O.; Tieleman, P.; Jähnig, F. Adhesion Forces of Lipids in a Phospholipid Membrane Studied by Molecular Dynamics Simulations. *Biophys. J.* **1998**, *74*, 931−943.
(62) Forest, L.; Sansom, M. S. Membrane Simulations: Bigger and Better? *Curr. Opin. Struct. Biol.* **2000**, *10*, 174−181.
(63) Mashl, R. J.; Scott, H. L.; Subramaniam, S.; Jakobsson, E. Molecular Simulation of Dioleoylphosphatidylcholine Lipid Bilayers at Differing Levels of Hydration. *Biophys. J.* **2001**, *81*, 3005−3015.
(64) Mukhopadhyay, P.; Monticelli, L.; Tieleman, D. P. Molecular Dynamics Simulation of a Palmitoyl-Oleoyl Phosphatidylserine Bilayer with Na+ Counterions and NaCl. *Biophys. J.* **2004**, *86*, 1601−1609.
(65) Sankararamakrishnan, R.; Weinstein, H. Surface Tension Parameterization in Molecular Dynamics Simulations of a Phospholipid-bilayer Membrane: Calibration and Effects. *J. Phys. Chem. B* **2004**, *108*, 11802−11811.
(66) Benz, R. W.; Castro-Román, F.; Tobias, D. J.; White, S. H. Experimental Validation of Molecular Dynamics Simulations of Lipid Bilayers: A New Approach. *Biophys. J.* **2005**, *88*, 805−817.
(67) Barzoukas, M.; Runser, C.; Fort, A.; Blanchard-Desce, M. A Two-State Description of (hyper) Polarizabilities of Push-Pull Molecules Based on a Two-Form Model. *Chem. Phys. Lett.* **1996**, *257*, 531−537.
(68) Klauda, J. B.; Venable, R. M.; Freites, J. A.; O'Connor, J. W.; Tobias, D. J.; Mondragon-Ramirez, C.; Vorobyov, I.; MacKerell, A. D., Jr.; Pastor, R. W. Update of the CHARMM All-Atom Additive Force Field for Lipids: Validation on Six Lipid Types. *J. Phys. Chem. B* **2010**, *114*, 7830−7843.
(69) Robinson, D.; Besley, N. A.; O'Shea, P.; Hirst, J. D. Di-8-ANEPPS Emission Spectra in Phospholipid/Cholesterol Membranes: A Theoretical Study. *J. Phys. Chem. B* **2011**, *115*, 4160−4167.
(70) Jämbeck, J. P. M.; Lyubartsev, A. P. Derivation and Systematic Validation of a Refined All-Atom Force Field for Phosphatidylcholine lipids. *J. Phys. Chem. B* **2012**, *116*, 3164−3179.
(71) Jurkiewicz, P.; Cwiklik, L.; Vojtíšková, A.; Jungwirth, P.; Hof, M. Structure, Dynamics, and Hydration of POPC/POPS Bilayers Suspended in NaCl, KCl, and CsCl Solutions. *Biochim. Biophys. Acta, Biomembr.* **2012**, *1818*, 609−616.
(72) Mori, T.; Miyashita, N.; Im, W.; Feig, M.; Sugita, Y. Molecular dynamics simulations of biological membranes and membrane proteins using enhanced conformational sampling algorithms. *Biochim. Biophys. Acta, Biomembr.* **2016**, *1858*, 1635−1651.
(73) Lyubartsev, A. P.; Rabinovich, A. L. Force Field Development for Lipid Membrane Simulations. *Biochim. Biophys. Acta, Biomembr.* **2016**, *1858*, 2483−2497.
(74) Macchiagodena, M.; Del Frate, G.; Brancato, G.; Chandramouli, B.; Mancini, G.; Barone, V. Computational study of the DPAP molecular rotor in various environments: from force field development to molecular dynamics simulations and spectroscopic calculations. *Phys. Chem. Chem. Phys.* **2017**, *19*, 30590−30602.
(75) Momany, F. A. Determination of Partial Atomic Charges from Ab Initio Molecular Electrostatic Potentials. Application to Formamide, Methanol, and Formic Acid. *J. Phys. Chem.* **1978**, *82*, 592−601.
(76) Singh, U. C.; Kollman, P. A. An Approach to Computing Electrostatic Charges for Molecules. *J. Comput. Chem.* **1984**, *5*, 129−145.
(77) Frisch, M. J.; et al. *Gaussian 16*, Revision A.03; Gaussian Inc.: Wallingford CT, 2016.
(78) Feller, S. E.; Zhang, Y.; Pastor, R. W.; Brooks, B. R. Constant Pressure Molecular Dynamics Simulation: The Langevin Piston Method. *J. Chem. Phys.* **1995**, *103*, 4613−4621.
(79) Piana, S.; Lindorff-Larsen, K.; Dirks, R. M.; Salmon, J. K.; Dror, R. O.; Shaw, D. E. Evaluating the Effects of Cutoffs and Treatment of Long-range Electrostatics in Protein Folding Simulations. *PLoS One* **2012**, *7*, No. e39918.
(80) Wang, J.; Wolf, R. M.; Caldwell, J. W.; Kollman, P. A.; Case, D. A. Development and Testing of a General Amber Force Field. *J. Comput. Chem.* **2004**, *25*, 1157−1174.
(81) Pizzirusso, A.; Savini, M.; Muccioli, L.; Zannoni, C. An Atomistic Simulation of the Liquid-Crystalline Phases of Sexithiophene. *J. Mater. Chem.* **2011**, *21*, 125−133.
(82) Pastor, R. W.; MacKerell, A. D., Jr. Development of the CHARMM Force Field for Lipids. *J. Phys. Chem. Lett.* **2011**, *2*, 1526−1532.
(83) Wu, Y.; Tepper, H. L.; Voth, G. A. Flexible Simple Point-Charge Water Model with Improved Liquid-State Properties. *J. Chem. Phys.* **2006**, *124*, 024503.
(84) Bersohn, R.; Pao, Y. H.; Frisch, H. L. Double-Quantum Light Scattering by Molecules. *J. Chem. Phys.* **1966**, *45*, 3184−3198.
(85) Mennucci, B.; Cancès, E.; Tomasi, J. Evaluation of Solvent Effects in Isotropic and Anisotropic Dielectrics and in Ionic Solutions with a Unified Integral Equation Method: Theoretical Bases, Computational Implementation, and Numerical Applications. *J. Phys. Chem. B* **1997**, *101*, 10506−10517.
(86) Tomasi, J.; Mennucci, B.; Cammi, R. Quantum Mechanical Continuum Solvation Models. *Chem. Rev.* **2005**, *105*, 2999−3094.
(87) Miertuš, S.; Scrocco, E.; Tomasi, J. Electrostatic Interactions of a Solute with a Continuum. A direct Utilization of Ab Initio Molecular Potentials for the Prevision of Solvent Effects. *Chem. Phys.* **1981**, *55*, 117−129.
(88) Oudar, J. L.; Chemla, D. S. Hyperpolarizabilities of the Nitroanilines and their Relations to the Excited State Dipole Moment. *J. Phys. Chem.* **1977**, *66*, 2664−2668.
(89) Lewis, B. A.; Engelman, D. M. Lipid bilayer thickness varies linearly with acyl chain length in fluid phosphatidylcholine vesicles. *J. Mol. Biol.* **1983**, *166*, 211−217.
(90) Chapman, D.; Williams, R. M.; Ladbrooke, B. D. Physical Studies of Phospholipids. VI. Thermotropic and Lyotropic Mesomorphism of some 1,2-diacyl-phosphatidylcholines (Lecithins). *Chem. Phys. Lipids* **1967**, *1*, 445−475.
(91) Levine, Y. K. Physical Studies of Membrane Structure. *Prog. Biophys. Mol. Biol.* **1972**, *24*, 1−74.
(92) Seelig, J.; Seelig, A. Lipid Conformation in Model Membranes and Biological Membranes. *Q. Rev. Biophys.* **1980**, *13*, 19−61.

https://dx.doi.org/10.1021/acs.jpcb.9b10988
J. Phys. Chem. B 2020, 124, 2101−2109